Article

Oxidant-Activated Reactions of Nucleophiles with Silicon Nanocrystals

Mita Dasog, Jonathan R Thompson, and Nathan S. Lewis

Chem. Mater., **Just Accepted Manuscript** • DOI: 10.1021/acs.chemmater.7b02572 • Publication Date (Web): 11 Jul 2017

Oxidant-Activated Reactions of Nucleophiles with Silicon Nanocrystals

Mita Dasog,[*1,2] Jonathan R. Thompson,[3] Nathan S. Lewis[*1,4,5]

[1]Division of Chemistry and Chemical Engineering, 210 Noyes Laboratory, California Institute of Technology, Pasadena, CA, USA

[2]Department of Chemistry, Dalhousie University, Halifax, NS, Canada

[3]Division of Engineering and Applied Sciences, California Institute of Technology, Pasadena, CA, USA

[4]Kavli Nanoscience Institute, California Institute of Technology, Pasadena, CA, USA

[5]Beckman Institute, California Institute of Technology, Pasadena, CA, USA

Abstract

The oxidant-activated reactivity of Si towards nucleophiles has been evaluated for Si nanocrystals (Si-NCs) of differing diameters, *d*. In the presence of ferrocenium as a one-electron, outer-sphere oxidant, Si-NCs with $d \geq 8$ nm readily reacted with nucleophiles including methanol, butanol, butylamine, butanoic acid, butylthiol, and diethylphosphine. However, Si-NCs with $d < 8$ nm did not undergo such reactions and stronger oxidants such as acetylferrocenium and 1,1'-diacetylferrocenium were required. Butylamine-, butylthiol-, and butanol- functionalized $d \geq 8$ nm Si-NCs were partially oxidized and exhibited photoluminescence originating from defect states. In contrast, butanoic acid-functionalized Si-NCs were minimally oxidized and displayed core emission resulting from the excitation and relaxation of electrons across the Si-NC bandgap. Diethylphosphine-functionalized Si-NCs were stable only under inert conditions, and showed core emission, with the Si-P bonds highly susceptible to oxidation and rapidly decomposing upon exposure to ambient conditions. The general reactivity is consistent with the redox potential of the one-electron oxidant and the valence band edge position of the Si-NCs. The trends in reactivity thus provide an example of differential chemical reactions of nanoparticles relative to bulk materials, reflecting the differences in electronic structure and continuum of electronic properties between variously sized Si nanoparticles and bulk Si samples.

Keywords: Silicon nanocrystals, quantum dots, semiconductors, surface chemistry, photoluminescence

1. Introduction

Quantum dots are promising optoelectronic materials, due to their tunable emission and absorption, multi-exciton generation, high emission quantum yields, and possibilities for inexpensive and scalable processing.[1–3] Silicon nanocrystals (Si-NCs) are of special interest due to the abundance, non-toxicity, and compatibility of Si with the existing semiconductor industry.[4,5] Modification of Si-NCs with organic functional groups minimizes surface oxidation, renders the particles dispersible, and adds desired functionality and solubility.[6] The most common method of surface modification involves the formation of Si-C bonds *via* hydrosilylation reactions in which terminal alkenes and alkynes are added to hydrogen-terminated silicon (Si) surfaces.[7] Alternative linkages to Si-NCs, such as Si-X (X= O, S),[8–11] Si–N,[12–15] and Si-Y (Y = Cl, Br, and I)[16,17] bonds, have also been developed. The nature of the Si linkage influences the electron transport, charge transfer, electronic structure, and photoluminescence properties of the nanocrystals.[12,18–22]

Si-NCs have generally been functionalized with Si-O bonds by reacting halide-terminated nanoparticles with alcohols or silanols.[15,23–25] Hydrogen-terminated Si surfaces also react with alcohols, albeit at a slow rate.[26,27] Ketones react with hydrogen-terminated Si-NCs to yield alkoxy functionalized surfaces.[28] Aldehydes react with bulk or porous Si-H surfaces,[29,30] but not with Si-NCs. Surface functionalization of Si/SiO_2 core-shell nanoparticles has been achieved *in-situ* during functionalization of Si-NCs with glutaric acid,[31] with the carboxylate group binding to the Si surface in a chelating fashion. Si-NCs that have Si-O linkages exhibit photoluminescence (PL) that is heavily influenced by oxygen defect states.[32–37] SiO_2 defects

typically result in both red and blue emission, whereas Si suboxide defects lead to orange-red PL.[12]

Si-N linkages can be made either by the direct reaction of Si-H with amines to yield hydrogen as the byproduct, or by the reaction of halide-terminated Si surfaces with amines.[12–14,38] The nitrogen-tethered Si-NCs usually exhibit blue PL from oxynitride defect states.[39] Thiol-capped Si-NCs have been prepared *via* high-temperature thiolation of the hydrogen-terminated Si surface.[9] Phosphine (PH_3) and diphosphine (P_2H_4) gas adsorption and decomposition has been investigated on bulk Si surfaces,[40–42] whereas reactions of alkylphosphines with Si surfaces, or formation of Si-P linkages in Si-NCs, are yet to be documented. Many of the reported methodologies for the formation of non-carbon Si linkages involve a halide intermediate that is difficult to produce in a nanocrystalline system given its propensity to etch the nanoparticles.[16] Direct reaction of Si-H surfaces with the desired ligands can be slow and/or lead to sub-surface oxidation and quenching of the nanocrystal PL.[43–45]

In contrast, alcohols readily (< 30 min) undergo oxidant-activated reactions with hydrogen-terminated Si(111) surfaces, and produce well-passivated surfaces.[46,47] A mechanistic study showed that such reactions proceed in the presence of acetylferrocenium, ferrocenium, or 1,1'-dimethylferrocenium as the oxidant.[48] In the dark, the reaction proceeds when both of the following conditions are satisfied: (i) the solution redox energy ($\mathbf{E}^{o}(A/A^{-})$) is negative of the surface resonance energy ($\mathbf{E}(Si^{+/0})$) and (ii) ($\mathbf{E}^{o}(A/A^{-})$) is near or negative of the valence band energy of Si ($\mathbf{E}_{vb}$).

We describe herein the acetyl-substituted and unsubstituted ferrocenium-activated reactivity of methanol with Si-NCs having diameters of d = 3 nm, 5 nm, or 8 nm, to explore variations in reactivity as a function of the energetics of the valence-band evolution in differently

sized Si nanoparticles. The scope of oxidant-activated Si surface functionalization has also been investigated beyond alcohols, including oxidant-activated reactions of nucleophiles such as amines, carboxylic acids, disulfides, and phosphines with hydrogen-terminated Si-NCs (**Scheme 1**).

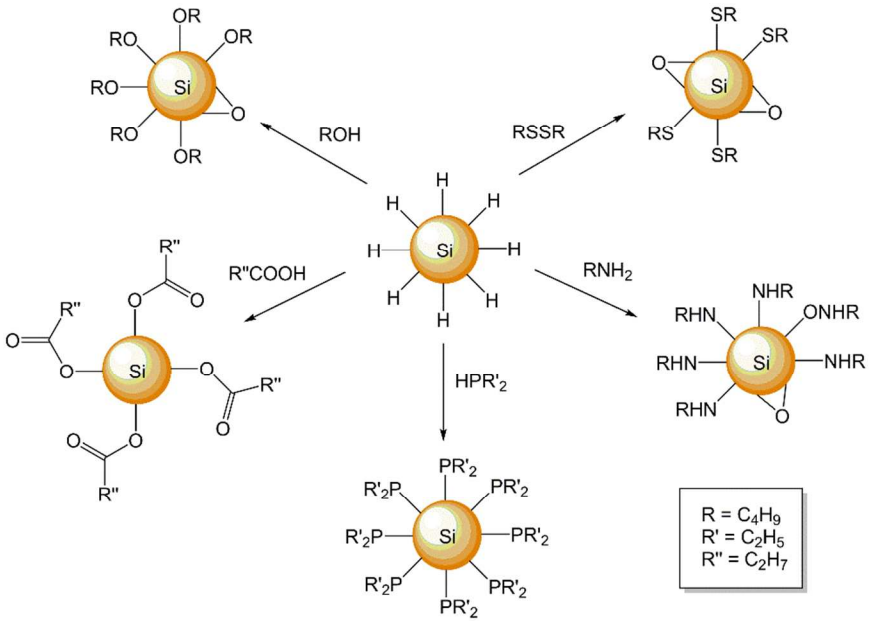

Scheme 1. Oxidant-activated reactivity of nucleophiles with hydrogen-terminated Si-NCs.

2. Experimental

2.1 Materials. Trichlorosilane ($HSiCl_3$, 99%), hydrofluoric acid (HF, 49%, J. T. Baker), toluene (≥99.5 %, ACS grade, Sigma-Aldrich), anhydrous methanol (≥99.5%, MeOH, Sigma-Aldrich), ethanol (99 %, EtOH, ACS grade, Sigma-Aldrich), anhydrous tetrahydrofuran (≥99.9%, THF, Sigma-Aldrich), butylamine (99.5%, Sigma-Aldrich), 1-butanol (99.4%, Sigma-Aldrich), 1-butanethiol (99%, Sigma-Aldrich), dibutyl disulfide (97%, Sigma-Aldrich), butanoic acid (≥99.5%, Sigma-Aldrich), acetylferrocene (95%, Sigma-Aldrich), 1, 1'-diacetylferrocene (97%,

Sigma-Aldrich) and diethylphosphine (98%, Sigma-Aldrich) were used without further purification. Ferrocenium ($Cp_2Fe^+BF_4^-$, bis(cyclopentadienyl)iron(III) tetrafluoroborate, technical grade, Sigma-Aldrich) was purified by recrystallization from diethyl ether (inhibitor-free, ≥99.9% Sigma-Aldrich) and CH_3CN (anhydrous, ≥99.8% Sigma-Aldrich). Water (≥18.2 MΩ cm resistivity) was obtained from a Barnstead E-Pure system.

2.2 Synthesis of oxide embedded silicon nanocrystals (Si-NCs). Oxide-embedded Si-NCs were prepared using a previously reported solid-state synthetic route by the disproportionation of polymeric $(HSiO_{1.5})_n$.[49,50] The $(HSiO_{1.5})_n$ polymer was prepared by addition, under N_2(g), of $HSiCl_3$ (4.5 mL, 45 mmol) to a flame-dried three-necked flask, followed by cooling the flask to 0 °C using an ice bath. Deionized water (1.59 mL, 90 mmol) was added to the $HSiCl_3$, and the reaction was warmed to room temperature and stirred for 1 h. One of the necks of the flask was used as a vent to remove the HCl by-product. The resulting white product was dried *in vacuo*, and the polymer was kept under an inert atmosphere, to prevent oxidation. The dried $(HSiO_{1.5})_n$ polymer was transferred to a quartz boat and heated in a tube furnace from ambient temperature to a peak processing temperature of 1100 °C, at 10 °C min^{-1}, under a reducing atmosphere (5% H_2/95% Ar). The sample was maintained at 1100 °C for 1 h and then cooled to room temperature. The resulting brown solid was ground using an agate mortar and pestle, yielding oxide-embedded Si-NCs with an average diameter of ~3 nm. To obtain larger Si-NCs, the 3 nm Si-NC composite was transferred to a carbon boat and heated in a high- temperature furnace for 1 h at 1200 °C or 1300 °C to yield Si-NCs with an average diameter of 5 nm and 8 nm, respectively.

2.3 Synthesis of hydrogen-terminated Si-NCs. Hydrogen-terminated Si-NCs were synthesized by treating 0.25 g of the oxide-embedded Si-NC composite with H_2O (3.0 mL), ethanol (3.0 mL), and 49% HF(aq) (3.0 mL), each for 1 h. The hydrophobic hydrogen-terminated Si-NCs

were extracted using 50.0 mL toluene. The Si-NC/toluene mixture was centrifuged for 15 min at 4000 rpm. The toluene supernatant was then decanted, leaving a precipitate of hydrogen-terminated Si-NCs. The particles were washed twice with toluene, and were immediately used for further reactions.

2.4 Oxidant-activated addition of methanol to hydrogen-terminated Si-NCs. Hydrogen-terminated Si-NCs (with d = 3 nm, 5 nm, or 8 nm) were re-dispersed in 25.0 mL of THF and transferred to an oven-dried Schlenk flask. The cloudy brown suspension was degassed using three freeze/pump/thaw cycles and maintained under a dry Ar(g) atmosphere. Similarly, methanol (1.00 mL) was degassed using three freeze/pump/thaw cycles and maintained under a dry Ar(g) atmosphere. The Si-NC-containing flask was covered with Al foil and 1.0 mM of the one-electron oxidant ($Cp_2Fe^+BF_4^-$, $(CpCOCH_3)CpFe^+$ or $(CpCOCH_3)_2Fe^+$) was added. Methanol was then transferred *via* cannula to the reaction flask, and the suspension was stirred for 30 min in the dark. The solution was then pumped down to remove THF and excess methanol. Ethanol (10.0 mL), toluene (0.5 mL), and methanol (1.0 mL) were added to the Si-NCs. and the solution was centrifuged for 15 min at 4000 rpm. The supernatant, which contained the reaction byproducts, was discarded. This washing process was repeated three times, with the Si-NC precipitate isolated and redispersed in THF for further characterization.

2.5 Oxidant-activated addition of nucleophile to hydrogen-terminated Si-NCs. The ~8 nm hydrogen-terminated Si-NCs (obtained from etching 0.25 g of the composite) were dispersed in 25.0 mL of THF and transferred to an oven-dried Schlenk flask. The cloudy brown suspension was degassed using three freeze/pump/thaw cycles and maintained under a dry Ar(g) atmosphere. 1.50 mL of the nucleophile (butanol, butylamine, butanoic acid, or dibutyl-disulfide) passed through an anhydrous $CaCl_2$ plug and degassed using three freeze/pump/thaw cycles and

maintained under a dry Ar(g) atmosphere. The Si-NC containing flask was covered with Al foil and $Cp_2Fe^+BF_4^-$ (0.30 g, 1.10 mmol) was added. The nucleophile was transferred *via* cannula to the reaction flask, and the suspension was stirred for 30 min in the dark. The solution was then pumped down to remove the THF. A mixture of solvents (details outlined in the Supporting Information) were added to the Si-NCs and the solution was centrifuged for 15 min at 4000 rpm. The supernatant that contained the reaction byproducts was discarded. The washing process was repeated twice, and the Si-NC precipitate was isolated and redispersed in THF for further characterization.

2.6 Oxidant-activated addition of diethylphosphine to hydrogen-terminated Si-NCs. The ~8 nm hydrogen-terminated Si-NCs (obtained from etching 0.15 g of the composite) were transferred to a N_2(g)-filled glovebox. The flask that contained the Si-NC solution was covered with aluminum foil and $Cp_2Fe^+BF_4^-$ (0.30 g, 1.10 mmol) and 25.0 mL of THF were added. 1.00 mL of diethylphosphine was added and the reaction mixture was stirred for 30 min in the dark. The solution was then pumped down to remove THF and excess phosphine. 15.0 mL of anhydrous acetone was added to the reaction mixture. The nanoparticle precipitate was isolated using vacuum filtration (which was performed in the glovebox). The Si-NCs were redispersed in hexanes, and care was taken to minimize exposure of the precipitate to air.

2.7 Control experiments. The ~ 8 nm hydrogen-terminated Si-NCs (obtained from etching 0.15 g of the composite) were dispersed in 25.0 mL of THF and transferred to an oven-dried Schlenk flask. The cloudy brown suspension was degassed using three freeze/pump/thaw cycles and maintained under a dry Ar(g) atmosphere. 1.50 mL of the nucleophile (except for diethylphosphine) was degassed using three freeze/pump/thaw cycles and maintained under a dry Ar(g) atmosphere. The solution was covered with Al foil, and the ligand was transferred *via*

cannula to the Si-NC solution and stirred for 30 min in the dark. The reaction mixture was centrifuged at 4000 rpm and the supernatant was discarded. The nanoparticles were washed with THF twice *via* centrifugation.

2.8 X-ray Photoelectron Spectroscopy (XPS). XPS analyses were performed using a Kratos Axis Ultra instrument operating in energy spectrum mode at 210 W. The base pressure and operating chamber pressure were maintained at 10^{-7} Pa. A monochromatic Al K_α source (λ = 8.34 Å) was used to irradiate the samples, and spectra were obtained with an electron takeoff angle of 90°. To minimize sample charging, the charge neutralizer filament was used. Survey spectra were collected using an elliptical spot with major and minor axis lengths of 2 and 1 mm, respectively, with a 160 eV pass energy and a step of 0.33 eV. CasaXPS software (VAMAS) was used to analyze the high-resolution (HR) XP spectra. All spectra were internally calibrated to the energy of the C 1s emission (284.8 eV) following the precedent for analysis of Si-NCs.[9,28,51,52] After calibration, the background was subtracted using a Shirley-type background to remove most of the extrinsic loss structure. The full width at half maximum (FWHM) for all of the fitted peaks was maintained below 1.5 eV.

2.9 Transmission Electron Microscopy (TEM). Low-magnification images were obtained using a Hitachi-9500 electron microscope with an accelerating voltage of 300 kV. High-resolution (HR) TEM images of thiol- and phosphine-stabilized Si-NCs were obtained using an FEI Tecnai F30ST microscope with an accelerating voltage of 300kV, whereas TEM images of butanol-, butanoic acid-, and butylamine-stabilized Si-NC were obtained on a Hitachi-9500 electron microscope with an accelerating voltage of 400 kV. TEM samples were prepared by drop coating the Si-NC suspension onto a carbon-coated Cu grid that had a 400 μm diameter

hole. The NC size was determined using Image J software (version 1.45). The HRTEM images were processed using Gatan DigitalMicrograph software (version 2.02.800.0).

2.10 Photoluminescence (PL). The PL spectra were acquired at room temperature using the 325 nm line of a He-Cd laser excitation source. The PL emission was detected with a fiber optic digital charge-coupled device (CCD) spectrometer whose spectral response was normalized using a standard blackbody radiator.

2.11 Infrared (IR) spectroscopy. The IR spectra were collected on a Nicolet 6700 spectrometer in ATR mode using a diamond window. The IR spectrum of phosphine-functionalized Si-NCs was obtained inside a N_2(g)-filled glovebox using a Cary 630 FTIR spectrometer in ATR mode, by drop casting the nanoparticles onto a diamond window.

3. Results

3.1 Influence of the nanoparticle size on oxidant-activated addition of methanol to hydrogen-terminated Si-NCs.

The disproportionation of $HSiO_{1.5}$ sol-gel polymer at high-temperature yields oxide embedded Si-NCs with diameters of 3.1 ± 0.6 nm, 5.2 ± 0.8 nm and 8.0 ± 1.3 nm (Figure S1) at 1100 °C, 1200 °C and 1300 °C, respectively. Hydrogen terminated Si-NCs were liberated from the oxide matrix using HF acid (Figure S2). Figure 1A shows the FT-IR spectra of Si-NCs of various sizes after ferrocenium- ($Cp_2Fe^+BF_4^-$) activated methoxylation of hydrogen-terminated Si-NCs in the dark and under an inert atmosphere. The 8 nm Si-NCs showed characteristic C-H stretches at ~ 2925 cm^{-1},[53] whereas the 3 nm and 5 nm diameter Si-NCs instead showed substantial Si-H_x stretches at ~ 2100 cm^{-1} and very weak C-H stretches at ~ 2925 cm^{-1}. Figure 1B shows

photographs of Si-NCs suspended in THF, before and after the methoxylation reaction. Hydrogen-terminated Si-NCs of all sizes appeared as cloudy suspensions. After the oxidant-activated methoxylation reaction, only the 8 nm nanoparticles appeared to be functionalized, yielding a clear orange-yellow solution when dispersed in THF, whereas both the 3 nm and 5 nm Si-NC solutions remained cloudy. In presence of the acetylferrocenium oxidant, Si-NCs with d = 8 nm and 5 nm reacted with methanol, as evidenced by the presence of C-H stretches ~ 2920 cm^{-1} and the absence of Si-H_x stretches ~ 2100 cm^{-1} (Figure S3). 1,1'-diacetylferrocenium effected the methoxylation of all three sizes of Si-NCs (Figure S3). The PL spectra (Figure S4) of methoxylated Si-NCs showed emission ca. 610 nm, 680 nm, and 730 nm for 3 nm, 5 nm, and 8 nm particles, respectively.

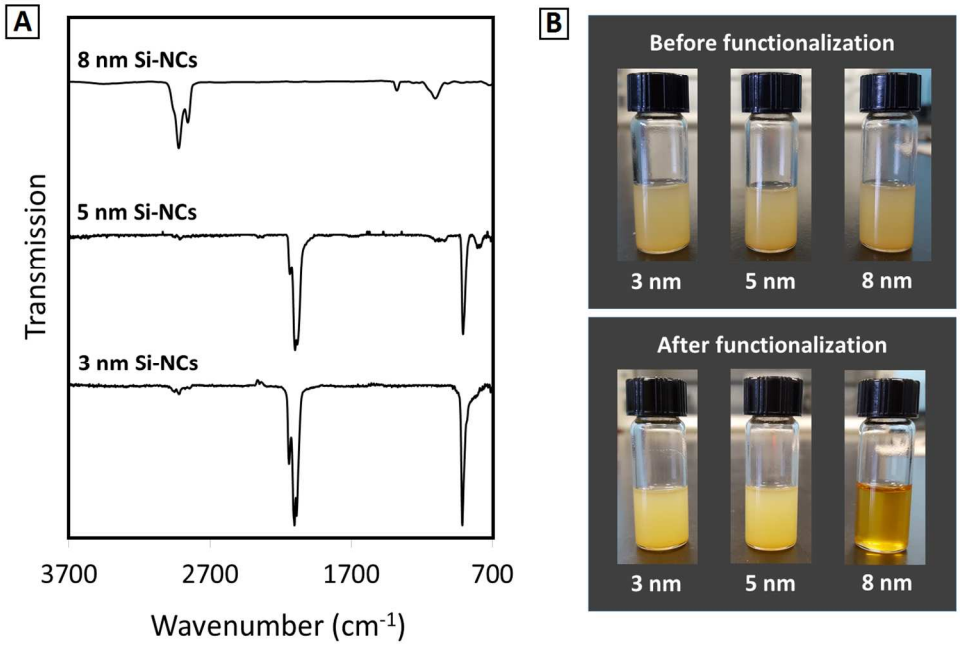

Figure 1. (A) FT-IR spectra of 3 nm, 5 nm, and 8 nm Si-NCs after ferrocenium activated methoxylation reaction. (B) Photographs of Si-NCs of various sizes in THF before (top) and after (bottom) the oxidant activated methoxylation reaction.

3.2 Oxidant-activated addition of butanol. After reaction with ferrocenium and butanol, the FT-IR spectrum of d = 8 nm butoxy-terminated Si-NCs showed C-H stretching (~ 2920 cm^{-1}) and bending vibrations (~ 1480 cm^{-1}) (Figure S5). A broad peak at ~ 1100 cm^{-1} likely originates from overlapping Si-O-Si and Si-O-C stretches[23] and a weak peak at ~ 2100 cm^{-1} is ascribable to residual Si-H_x stretching intensity.

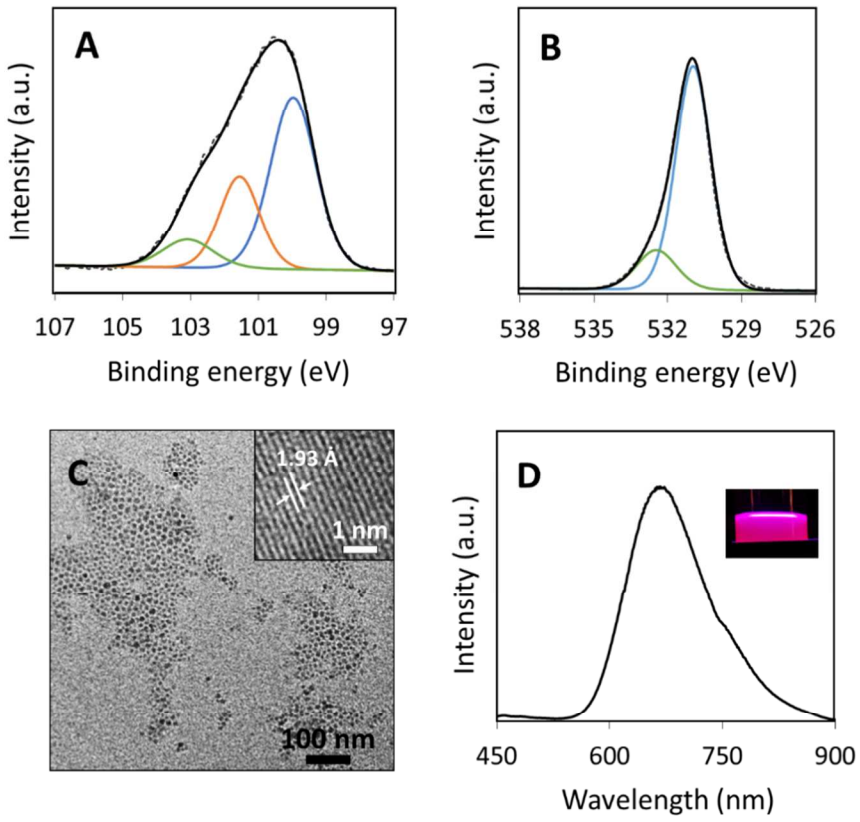

Figure 2. Characterization of butoxy-functionalized Si-NCs. High-resolution XP spectra of (A) Si 2p and (B) O 1s regions (the solid black line corresponds to the fitted spectrum. For clarity, only $2p_{3/2}$ fitted peaks are shown). (C) Transmission-electron micrograph (inset: high-resolution TEM showing characteristic 220 crystal plane of Si). (D) PL spectrum at λ_{ex} = 325 nm (inset: photograph of Si-NCs in THF under UV-illumination).

The high-resolution Si 2p XP spectrum of butanol-functionalized Si-NCs was well-fit with six peaks with $2p_{3/2}$ ca. 99.9 eV, 101.5 eV, and 103.0 eV, corresponding to Si(0) atoms, butoxy-bonded surface Si atoms, and Si suboxide species, respectively (Figure 2A).[54,55] The O 1s XP spectrum (Figure 2B) displayed two emission peaks, at 532.5 eV and 531.0 eV, corresponding to O in butanol and Si suboxide, respectively.[56,57] Representative TEM images of butoxy- functionalized Si-NCs (Figure 2C) showed particles with an average diameter of 8.1 ± 1.2 nm. These Si-NCs showed red PL at ~ 670 nm (Figure 2D). Hydrogen-terminated Si-NCs were also reacted with butanol in absence of the ferrocenium and the FT-IR spectrum (Figure S6) showed Si-H_x stretches at 2080 cm^{-1} and 900 cm^{-1} and Si-O-Si stretches at 1095 cm^{-1}.

3.3 Oxidant-activated addition of butylamine. After reaction with butylamine in the presence of ferrocenium as the oxidant, FT-IR spectra of functionalized d = 8 nm Si-NCs (Figure S7) showed characteristic C-H stretching (~2900 cm^{-1}) and bending vibrations (~1480 cm^{-1}). N-H stretching, bending, and wagging modes were also present at 3300 cm^{-1}, 1700 cm^{-1}, and 810 cm^{-1}, respectively,[12] with C-N and Si-O-Si stretches observed at 1300 cm^{-1} and 1080 cm^{-1}, respectively.

The high-resolution Si 2p XP spectrum of butyl-amine-functionalized Si-NCs was well-fit by eight peaks with $2p_{3/2}$ at 99.9 eV, 101.1 eV, 102.0 eV and 103.0 eV, corresponding to Si(0) atoms, surface Si bonded to an amine functional group, Si oxynitride species, and Si suboxide, respectively (Figure 3A). The N 1s XP spectrum (Figure 3B) consisted of two emission peaks, at 399.0 eV and 400.1 eV, corresponding to Si-N and Si-O-N, respectively.[13] TEM images of butylamine- functionalized Si-NCs (Figure 3C) showed particles with an average diameter of 8.0 ± 1.1 nm. These Si-NCs exhibited blue PL at ~405 nm (Figure 3D). Hydrogen-terminated Si-NCs were also reacted with butylamine in absence of the ferrocenium. The FT-IR spectrum

(Figure S8) showed Si-H_x stretches at 2100 cm^{-1} and 910 cm^{-1} and Si-O-Si stretches at 1090 cm^{-1}, with C-H (2950 and 1420 cm^{-1}), N-H (3330 and 1710 cm^{-1}), and C-N (1310 cm^{-1}) stretches also observed.

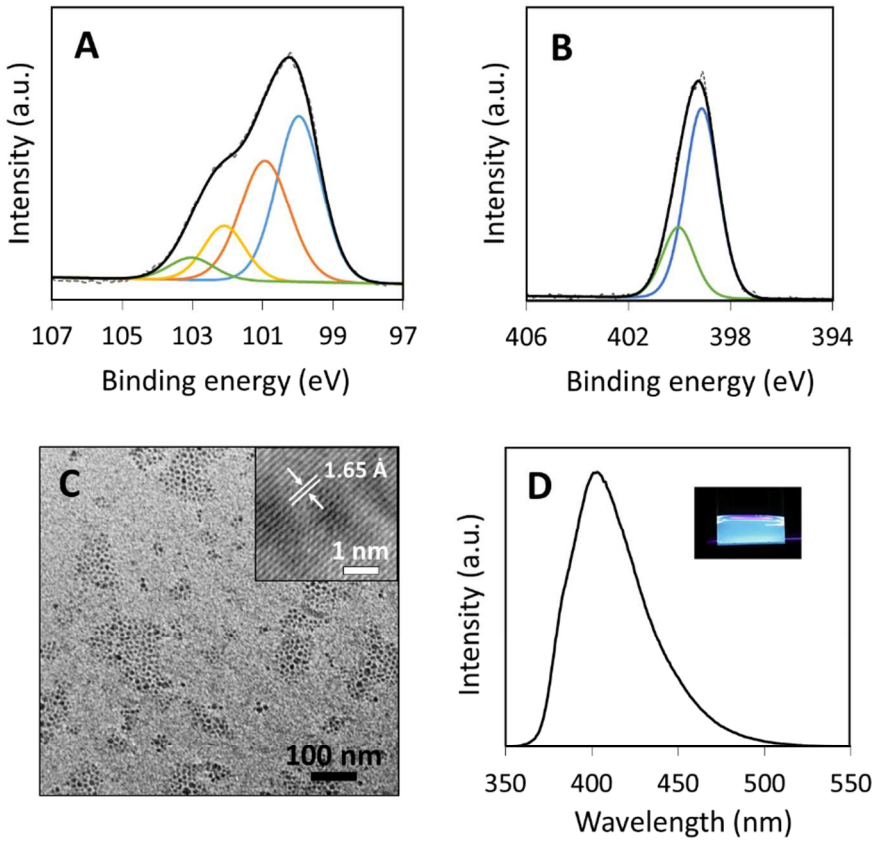

Figure 3. Characterization of butylamine-functionalized Si-NCs. High-resolution XP spectra of (A) Si 2p and (B) N 1s regions (the solid black line corresponds to the fitted spectrum. For clarity, only $2p_{3/2}$ fitted peaks are shown). (C) Transmission-electron micrograph (inset: high-resolution TEM showing characteristic 311 crystal plane of Si). (D) PL spectrum at λ_{ex} = 325 nm (inset: photograph of Si-NCs in THF under UV-illumination).

3.4 Oxidant-activated addition of butanoic acid. After reaction with ferrocenium and butanoic acid, the FT-IR spectrum of 8 nm diameter Si-NCs (Figure S9) showed characteristic C-H

stretching (~ 2900 cm^{-1}) and bending vibrations (~ 1450 cm^{-1}). Sharp C=O and C-O stretches were observed at 1750 cm^{-1} and 1220 cm^{-1}, respectively,[58] and a peak at 1020 cm^{-1} likely originates from Si-carboxylic acid (Si-O) linkages.

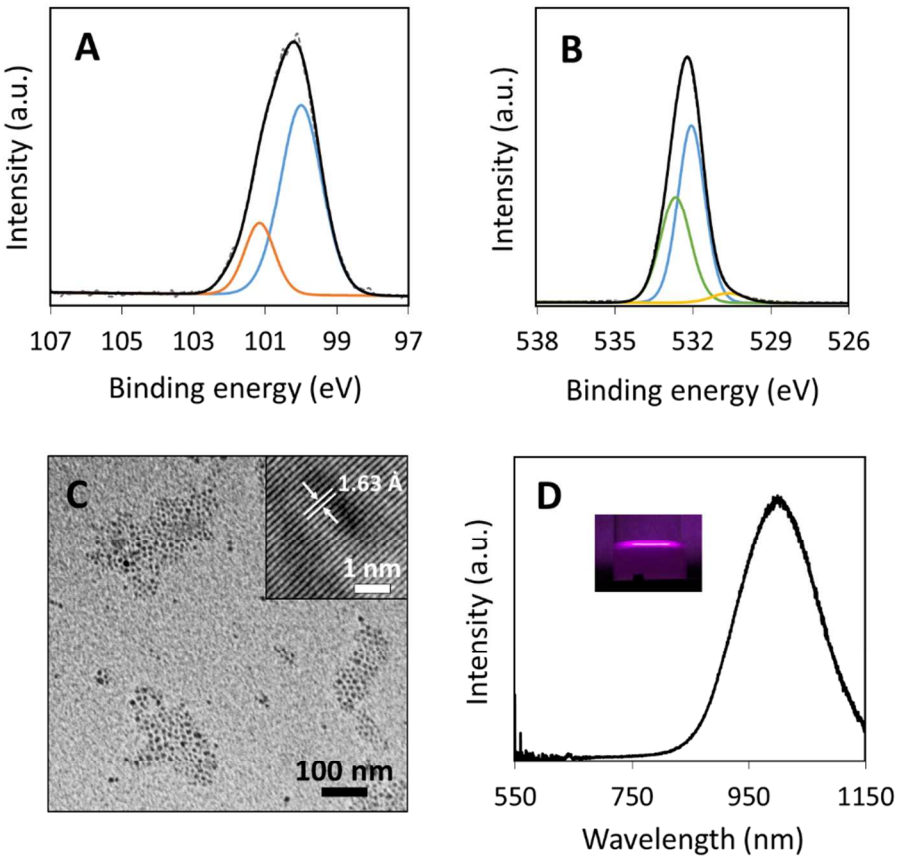

Figure 4. Characterization of butanoic acid functionalized Si-NCs. High-resolution XP spectra of (A) Si 2p and (B) O 1s regions (the solid black line corresponds to the fitted spectrum. For clarity, only $2p_{3/2}$ fitted peaks are shown). (C) Transmission-electron micrograph (inset: high-resolution TEM showing characteristic 311 crystal plane of Si). (D) PL spectrum at λ_{ex} = 325 nm (inset: photograph of Si-NCs in THF under UV-illumination).

The high-resolution Si 2p XP spectrum of the butanoic acid-functionalized Si-NCs exhibited four emission peaks with $2p_{3/2}$ at 99.9 eV and 101.2 eV, corresponding to Si(0) atoms

and butanoic acid bonded Si, respectively (Figure 4A). The O 1s XP spectrum (Figure 4B) contained emission peaks at 531.0 eV and 532.5 eV, corresponding to silicon-bound O atoms and doubly bonded O in carboxylic acid, respectively. The origin of the peak at 530.6 eV currently remains unclear. TEM images of butanoic acid functionalized Si-NCs (Figure 4C) showed particles with an average diameter of 8.0 ± 1.0 nm. These Si-NCs showed near-IR PL at ~1005 nm (Figure 4D). Hydrogen-terminated Si-NCs were also reacted with butanoic acid in absence of the ferrocenium. The FT-IR spectrum (Figure S10) showed Si-H_x stretches at 2100 cm^{-1} and 910 cm^{-1}, as well as a Si-O-Si stretch at 1100 cm^{-1}.

3.5 Oxidant-activated addition of dibutyl-disulfide. In the presence of ferrocenium, no reaction was observed between butylthiol and Si-NCs. Dibutyl-disulfide was therefore instead added to 8 nm hydrogen-terminated Si-NCs in the presence of ferrocenium as the oxidant, to prepare thiol-stabilized Si-NCs. The FT-IR spectrum of the butylthiol-functionalized Si-NCs showed characteristic C-H stretching (~ 2950 cm^{-1}) and bending vibrations (~ 1490 cm^{-1}) (Figure S11). A broad peak at ~1100 cm^{-1} originated from Si-O-Si stretches, whereas a weak peak was observed at ~2100 cm^{-1} from the residual Si-H_x stretches. The high-resolution Si 2p XP spectrum exhibited six emission peaks with $2p_{3/2}$ at 99.8 eV, 101.0 eV, and 103.6 eV, corresponding to Si(0) atoms, thiol-bound Si surface atoms, and Si suboxide, respectively (Figure 5A).[58] The S 2p XP spectrum (Figure 5B) showed a $2p_{3/2}$ peak at ~163.0 eV, characteristic of Si-bound S atoms.[59,60] TEM images of butylthiol-functionalized Si-NCs (Figure 5C) showed particles with an average diameter of 7.9 ± 1.3 nm. These Si-NCs show red emission at ~650 nm (Figure 5D). Hydrogen-terminated Si-NCs were also reacted with dibutyl disulfide in the absence of the ferrocenium. The FT-IR spectrum (Figure S12) showed Si-H_x stretches at 2100 cm^{-1} and 906 cm^{-1} and Si-O-Si stretches at 1080 cm^{-1}.

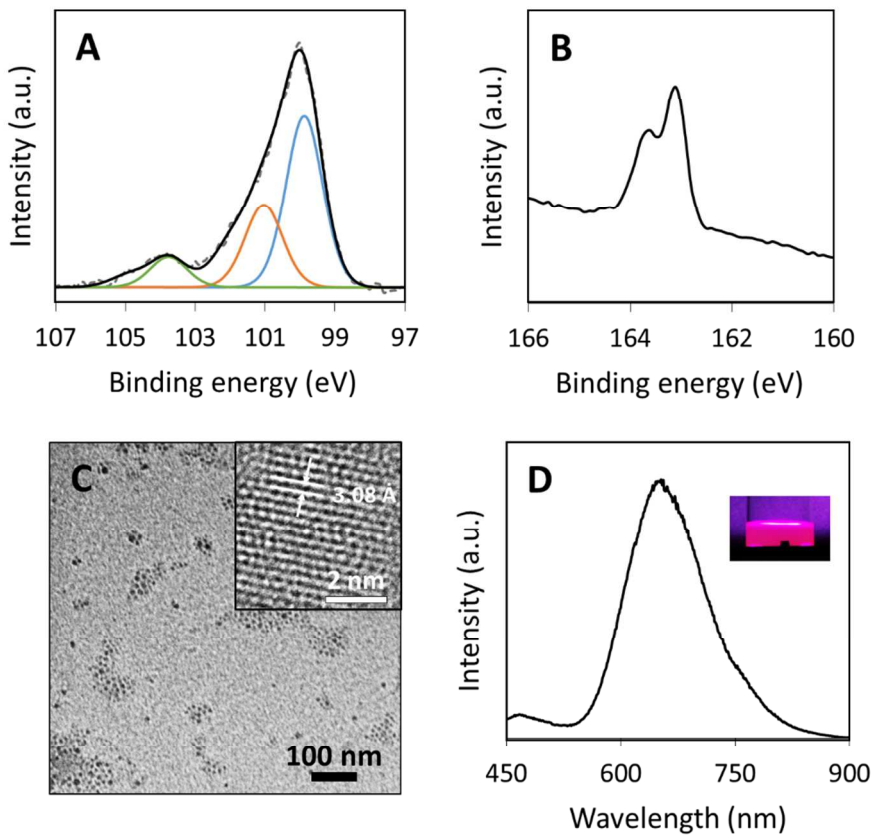

Figure 5. Characterization of butylthiol-functionalized Si-NCs. High-resolution XP spectra of (A) Si 2p and (B) S 2p regions (the solid black line in Si peak corresponds to the fitted spectrum. For clarity, only $2p_{3/2}$ fitted peaks are shown). (C) Transmission-electron micrograph (inset: high-resolution TEM showing characteristic 111 crystal plane of Si). (D) PL spectrum at λ_{ex} = 325 nm (inset: photograph of Si-NCs in toluene under UV-illumination).

3.6 Oxidant-activated addition of diethylphosphine. In the presence of ferrocenium as the oxidant, but with minimum exposure to air and moisture, the FT-IR spectrum of 8 nm Si-NCs functionalized with diethylphosphine showed characteristic C-H stretching (~ 2930 cm^{-1}) and bending vibrations (~ 1425 cm^{-1}) (Figure S13). The high-resolution Si 2p XP spectrum (Figure 6A) exhibited six emission peaks with $2p_{3/2}$ at 99.9 eV, 101.6 eV, and 104.6 eV, corresponding to Si(0) atoms, phosphine bonded Si atoms, and SiO_2, respectively. The P 2p XP spectrum (Figure 6B) showed a $2p_{3/2}$ peak at 129.0 eV, characteristic of P atoms bound to Si.[61] TEM

images of phosphine-functionalized Si-NCs (Figure 6C) showed particles with an average diameter of 8.1 ± 1.1 nm that exhibited near-IR PL at ~ 990 nm (Figure 6D). Upon exposure to ambient conditions, the phosphine-stabilized Si-NC surfaces decomposed rapidly, leading to precipitation of the nanocrystals (Figure S14). Hydrogen-terminated Si-NCs were also reacted with diethylphosphine in absence of the ferrocenium. The FT-IR spectrum (Figure S15) showed Si-H_x stretches at 2085 cm^{-1} and 910 cm^{-1} and Si-O-Si stretches at 1070 cm^{-1}.

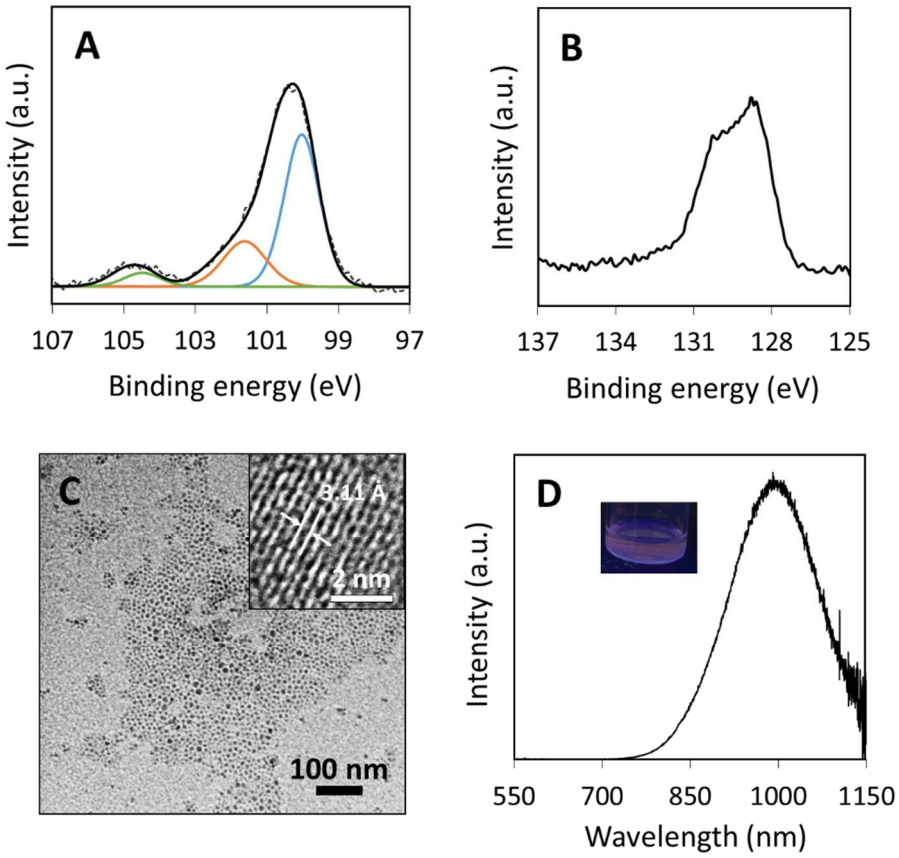

Figure 6. Characterization of diethylphosphine-functionalized Si-NCs. High-resolution XP spectra of (A) Si 2p and (B) P 2p regions (the solid black line in Si peak corresponds to the fitted spectrum. For clarity, only $2p_{3/2}$ fitted peaks are shown). (C) Transmission-electron micrograph (inset: high-resolution TEM showing characteristic 111 crystal plane of Si). (D) PL spectrum at λ_{ex} = 325 nm (inset: photograph of Si-NCs in hexanes under UV-illumination).

4. Discussion

4.1. Size Dependence of Oxidant-Induced Reactivity of Nucleophiles

Only the larger Si-NCs underwent ferrocenium-activated surface modification, as evidenced by the appearance of C-H stretches and the absence of Si-H stretches in the FT-IR spectrum (Figure 1A). The reactivity was further confirmed by the visual appearance of the NC solution, with only the 8 nm Si-NCs being dispersible in THF whereas 5 nm and 3 nm Si-NC suspensions remained cloudy after the reaction (Figure 1B). A slight reaction between methanol and Si-hydrogen surface may occur without the aid of the oxidant, as evidenced by the presence of very weak C-H stretches (Figure 1) but this pathway contributes < 5% surface coverage. Stronger oxidants, acetylferrocenium and 1,1'-diacetylferrocenium, were required to methoxylate 5 nm and 3 nm Si-NCs, respectively. The size dependence of the oxidant-activated methoxylation of Si-NCs is consistent with a recently proposed mechanism for the reaction.[48] The band edge positions of nanocrystalline Si have been previously determined using various techniques, such as scanning- tunneling microscopy (STM), UV-photoelectron spectroscopy (UPS), and absorption and emission spectra.[62–67] However, these techniques are highly sensitive to sample preparation, substrates, and surface chemistry. Calculations performed by Hill *et al*. have shown that the shift in valence band edge of Si-NCs is approximately twice as large as the shift in the conduction-band edge.[68]

Based on these calculations, the band edge positions for Si-NCs of different sizes are shown in Figure 7. The redox potential of $Cp_2Fe^{+/o}$ relative to the Si valence-band edge was obtained from previous work.[69] The band gaps of the nanocrystals were determined using a sizing curve developed by Wheeler *et al*. (Equation 1):[70]

$$E(d) = 1.12 + 3.73d^{-1.69} \qquad \text{(Equation 1)}$$

where d is the nanocrystal diameter. The band gaps of the nanocrystals were calculated to be 1.23 eV, 1.35 eV, and 1.67 eV for d = 8.0 nm, 5.2 nm, and 3.1 nm Si-NCs, respectively. PL studies of hydrogen-terminated Si-NCs (Figure S16) yielded optical band gaps 1.70 eV, 1.40 eV, and 1.24 eV for 3.1 nm, 5.2 nm, and 8.0 nm particles, respectively, which are within standard deviation of the NC sizes.

The oxidant-activated methoxylation reaction proceeds when (i) the solution redox energy ($\mathbf{E}^o(A/A^-)$) is negative of the surface resonance energy ($\mathbf{E}(Si^{+/0})$) and (ii) the valence band edge of Si is near or positive of the redox energy of the solution ($\mathbf{E}^o(A/A^-)$). The surface resonance energy ($\mathbf{E}(Si^{+/0})$) lies at approximately -4.7 eV. Therefore, the first condition is satisfied for all NC sizes. For bulk Si and larger Si-NCs (8 nm), the valence band edges are at -5.17 eV and -5.24 eV, respectively, which is close to the redox energy of $Cp_2Fe^{+/o}$. However, the valence-band edges shift to -5.36 eV and -5.54 eV for 5 nm and 3 nm Si-NCs, respectively, which are too negative with respect to $Cp_2Fe^{+/o}$ for effective transfer of the electrons from Si to the oxidant. Consistently, methoxylation was only observed for the 8 nm Si-NCs in presence of ferrocenium. The redox energy of acetylferrocene/acetylferrocenium ($(CpCOCH_3)CpFe^{+/0}$) is closer to the 5 nm Si-NC valence band edge and positive of 8 nm Si-NC valence band edge, thus facilitating methoxylation of both 5 nm and 8 nm Si-NCs. The strongest oxidant used in this study, 1,1'-diacetylferrocenium, methoxylated all sizes of Si-NCs, because the redox energy of 1,1'-diacetylferrocene/1,1'-diacetylferrocenium ($(CpCOCH_3)_2Fe^{+/0}$) is favorably positioned for electron transfer from Si to the oxidant.

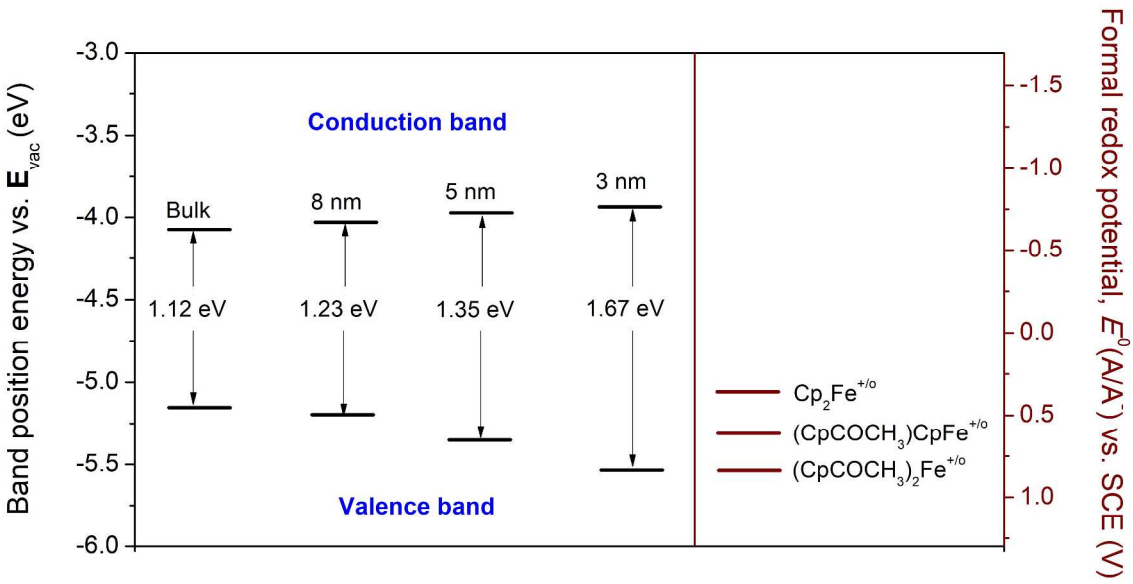

Figure 7. Relative energy positions of the valence- and conduction-band edges of bulk and nanocrystalline Si vs. the vacuum level and formal potential of $Cp_2Fe^{+/o}$, $(CpCOCH_3)CpFe^{+/0}$, $(CpCOCH_3)_2Fe^{+/0}$ vs. SCE.

Size-dependent reactivity has previously been observed for near-UV photochemical hydrosilylation of Si-NC surfaces.[71,72] Smaller NCs undergo efficient hydrosilylation due to the formation of a transition state that is favored in higher band gap Si-NCs. Although the energy difference between the valence and conduction bands is important for such photochemical reactions, the actual positioning of the valence and conduction band edges does not influence the surface reactivity. In another study, the influence of Si-NC size on surface oxidation in presence of water and oxygen was investigated.[73] The larger particles exhibited higher oxidation, due to their lower band gap and thus lower ionization potential. However, the position of the band edges was not a major factor. In contrast, the reactivity described herein allows for qualitative

chemical mapping of the energy of the valence band edges of the variously sized Si-NCs and size selective surface functionalization.

4.2. General Trends in the Oxidant-Activated Nucleophilic Reactivity of Si

The ferrocenium-activated reaction of hydrogen-terminated Si-NCs (d ~ 8 nm) was expanded beyond methanol, to include other nucleophiles such as butanol, butylamine, butanoic acid, dibutyl disulfide, and diethylphosphine. Butanol reacted with 8 nm Si-NCs in presence of ferrocenium, as confirmed by the presence of C-H and Si-O-C stretches in the FT-IR spectrum (Figure S5). Partial oxidation of the Si surface was observed by the presence of Si-O-Si stretches in the FT-IR spectrum and emission peaks in Si 2p and O 1s XPS (Figure 2A and B). The NCs also showed red PL originating from the Si suboxide defect states.[12,74] No functionalization of Si surfaces was observed with butanol in the absence of ferrocenium, as confirmed by FT-IR spectroscopy (Figure S6).

Similarly, butylamine also added to hydrogen-terminated 8 nm Si-NCs in presence of ferrocenium. The functionalization was confirmed by the presence of Si-N emission peaks in Si 2p and N 1s XPS (Figure 3A and B) and C-H stretches in the FT-IR spectrum (Figure S7). These nanoparticles showed partial oxidation and the presence of oxynitride moieties, as confirmed by the XPS analysis. Butylamine-stabilized Si-NCs showed blue PL resulting from the charge-transfer process between Si-NC and the oxynitride defect state that has been identified in amine stabilized Si-NCs.[13,75] The reaction of butylamine with hydrogen-terminated Si-NCs proceeded even in the absence of ferrocenium, by forming hydrogen as the byproduct. However, the surface coverage was lower and surface oxidation was higher in the absence of ferrocenium. This difference in surface reactivity affects the long-term stability of the NCs, and after two weeks the

NC's precipitated out of the solution (Figure S17), whereas Si-NCs functionalized in presence of ferrocenium remained dispersible over time scales in excess of 2-3 months.

Ab initio studies predict that carboxylic acid-stabilized Si surfaces should be thermodynamically very stable, and very well-ordered surfaces should be obtainable.[76] Through the oxidant-activated route, butanoic acid reacted with the Si-NC surface, as confirmed by the presence of C-H, C=O, and Si-O-C stretches in FT-IR spectrum (Figure S9). Unlike oxidatively activated reaction with butanol and butylamine, partial oxidation was not observed for these NCs. It is possible the carboxylate ligand binds to the Si surface in a chelating fashion, thus sterically preventing water or oxygen molecules from attacking the surface. The emission properties of butanoic acid-stabilized Si-NCs was not dominated by the defect states, and instead a PL peak was observed with an emission maximum of ~1005 nm. The energy of this emission corresponds well with the excitation and relaxation of the electrons across the NC bandgap.[77] Butanoic acid led to well-passivated Si-NCs that were air-stable and exhibited band-gap emission. In the absence of ferrocenium, butanoic acid did not react with hydrogen-terminated Si-NCs (Figure S10).

Ferrocenium-activated addition of thiols to hydrogen-terminated Si-NC surfaces was attempted using butylthiol. However, in presence of ferrocenium, the butylthiol oxidized to yield disulfide and unfunctionalized Si-NCs (Scheme 2). Dibutyl-disulphide was thus used instead of the thiol, because the oxidation potential of the disulfide is more positive than that of the thiol.[78] Thiol-stabilized Si-NCs were then readily obtained *via* the ferrocenium-activated route, with functionalization confirmed by the Si-S signal in the Si 2p and S 2p XPS regions (Figure 5A and B). However, similar to the reactivity observed with butanol, partial surface oxidation was

observed in thiolated Si-NCs, with suboxide defect emission at ~ 650 nm. No reaction was observed in absence of ferrocenium between dibutyl-disulfide and Si-NCs.

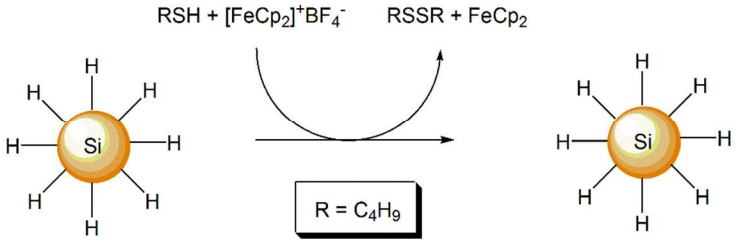

Scheme 2. Reaction of butylthiol with hydrogen-terminated Si-NCs in the presence of ferrocenium as the oxidant.

Diethylphosphine also readily reacted as a nucleophile to functionalize 8 nm Si-NCs in the presence of ferrocenium. This reaction was extremely sensitive to air and moisture, due to pyrophoric nature of the phosphine. The functionalization was confirmed by the presence of Si-P emission peaks in the Si 2p and P 2p regions of the XPS (Figure 6A and B) as well as by the C-H stretches in the IR spectrum (Figure S13). No surface oxidation was observed in the IR spectrum, but SiO_2 was observed in the Si 2p region by XPS. Oxidation could have occurred in the short time that the sample was transferred from the glove box to the XPS sample chamber. The oxide-free phosphine-protected Si-NCs showed near-IR emission, resulting from the excitation and relaxation of charge-carriers across the Si-NC band gap. The NCs decomposed rapidly, however, when exposed to air. Diethylphosphine did not react with hydrogen-terminated Si-NCs in the absence of ferrocenium.

The PL properties of the functionalized Si-NCs discussed here provide some insight into the quality of the surface passivation. The carboxylic acid passivated and protected the Si surface

most effectively with other heteroatom ligands introducing partial oxidation and surface defect sites.

5. Conclusions

Oxidant-activated addition of methanol to Si-NCs with average diameters of 3 nm, 5 nm, and 8 nm was investigated, and only larger (8 nm) Si-NCs underwent methoxylation in presence of ferrocenium. Stronger oxidants such as acetyl and 1,1'-diacetylferrocenium were required for the smaller Si-NCs. The observations are consistent with the valence band edge of the Si-NCs being closer to the redox potential of the respective oxidants. The scope of the reaction was expanded to other nucleophiles, and butanol-, butylamine- butylthiol-, butanoic acid-, and diethylphosphine-stabilized Si-NCs were prepared in presence of ferrocenium as the oxidant. Functionalization of Si-NC surfaces with these nucleophiles was confirmed using FT-IR and XPS techniques. Butanol- and butylthiol-stabilized Si-NCs exhibited red PL originating from suboxide defect states, whereas butylamine-stabilized Si-NCs exhibited blue PL resulting from an oxynitride defect state. Butanoic acid-stabilized Si-NCs were oxide free and showed size-dependent emission resulting from the band gap. Diethylphosphine-stabilized Si-NCs also showed size-dependent PL but were only stable under inert conditions and decomposed rapidly upon exposure to air. The oxidant-activated route opens a versatile synthetic route to add, in one step, sugars, peptides, DNA, RNA, and other complex molecules that contain alcohol, amines, thiols, or carboxylic acid functional groups to Si-NC surfaces.

ASSOCIATED CONTENT

Supporting Information

The supporting information is available free of charge on the ACS publications website at DOI: Supporting Figures S1–S18 and experimental details for the in-situ generation of the acetyl and dicetyl ferrocenium and purification of various functionalized Si-NCs.

AUTHOR INFORMATION

Corresponding Author

*(N.S.L.) E-mail: nslewis@caltech.edu; Tel: (626) 395-6335

*(M.D.) E-mail: mita.dasog@dal.ca; Tel: (902) 494-4245

Notes

The authors declare no competing financial interest.

ACKNOWLEDGEMENTS

The authors acknowledge the National Science Foundation, grant CHE-1214152, and Dalhousie University for providing financial support. Instrumentation support was provided by the Molecular Materials Research Center of the Beckman Institute at the California Institute of Technology and by the Institute for Research in Materials at Dalhousie University. M.D. acknowledges a postdoctoral fellowship from the National Sciences and Engineering Research Council of Canada. J. R. T. acknowledges support from DOE "Light-Material Interactions in Energy Conversion" Energy Frontier Research Center under grant DE-SC0001293. We thank Dr. A. C. Nielander and Azhar Carim for insightful discussions during the preparation of this work.

References.

(1) Freeman, R.; Willner, I. Optical molecular sensing with semiconductor quantum dots. *Chem. Soc. Rev.* **2012**, *41*, 4067-4085.

(2) Zhou, J.; Yang, Y.; Zhang, C. Y. Toward biocompatible semiconductor quantum dots: from biosynthesis to biomedical application. *Chem. Rev.* **2015**, *115*, 11669-11717.

(3) Nozik, A. J.; Beard, M. C.; Luther, J. M.; Law, M.; Ellingson, R. J.; Johnson, J. C. Semiconductor quantum dots and quantum dot arrays and applications of multiple exciton generation to third-generation photovoltaic solar cells. *Chem. Rev.* **2010**, *110*, 6873-6890.

(4) Cheng, X.; Lowe, S. B.; Reece, P. J.; Gooding, J. J. Colloidal silicon quantum dots: from preparation to the modification of self-assembled monolayers (SAMs) for bio-applications. *Chem. Soc. Rev.* **2014**, *43*, 2680-2700.

(5) Reiss, P.; Carrière, M.; Lincheneau, C.; Vaure, L.; Tamang, S. Synthesis of semiconductor nanocrystals, focusing on nontoxic and earth-abundant materials. *Chem. Rev.* **2016**, *116*, 10731-10819.

(6) Dasog, M.; Kehrle, J.; Rieger, B.; Veinot, J. G. C. Silicon nanocrystals and silicon-polymer hybrids: synthesis, surface engineering, and applications. *Angew. Chemie. Int. Ed.* **2016**, *55*, 2322-2339.

(7) Buriak, J. M. Illuminating silicon surface hydrosilylation: an unexpected plurality of mechanisms. *Chem. Mater.* **2014**, *26*, 763-772.

(8) Veinot, J. G. C. Synthesis, surface functionalization, and properties of freestanding silicon

nanocrystals. *Chem. Commun.* **2006**, 4160-4168.

(9) Yu, Y.; Rowland, C. E.; Schaller, R. D.; Korgel, B. A. Synthesis and ligand exchange of thiol-capped silicon nanocrystals. *Langmuir* **2015**, *31*, 6886-6893.

(10) Pettigrew, K. A.; Liu, Q.; Power, P. P.; Kauzlarich, S. M. Solution synthesis of alkyl- and alkyl/alkoxy-capped silicon nanoparticles via oxidation of Mg_2Si. *Chem. Mater.* **2003**, *15*, 4005-4011.

(11) Li, X.; He, Y.; Swihart, M. T.; and Mark T. Swihart. Surface functionalization of silicon nanoparticle produced by laser-driven pyrolysis of silane followed by HF-HNO_3. *Langmuir* **2004**, *20*, 4720-4727.

(12) Dasog, M.; De Los Reyes, G. B.; Titova, L. V.; Hegmann, F. A.; Veinot, J. G. C. Size vs surface: tuning the photoluminescence of freestanding silicon nanocrystals across the visible spectrum via surface groups. *ACS Nano* **2014**, *8*, 9636-9648.

(13) Dasog, M.; Yang, Z.; Regli, S.; Atkins, T. M.; Faramus, A.; Singh, M. P.; Muthuswamy, E.; Kauzlarich, S. M.; Tilley, R. D.; Veinot, J. G. C. Chemical insight into the origin of red and blue photoluminescence arising from freestanding silicon nanocrystals. *ACS Nano* **2013**, *7*, 2676-2685.

(14) Li, Q.; He, Y.; Chang, J.; Wang, L.; Chen, H.; Tan, Y. W.; Wang, H.; Shao, Z. Surface-modified silicon nanoparticles with ultrabright photoluminescence and single-exponential decay for nanoscale fluorescence lifetime imaging of temperature. *J. Am. Chem. Soc.* **2013**, *135*, 14924-14927.

(15) Zhai, Y.; Dasog, M.; Snitynsky, R. B.; Purkait, T. K.; Aghajamali, M.; Hahn, A. H.;

Sturdy, C. B.; Lowary, T. L.; Veinot, J. G. C. Water-soluble photoluminescent d-mannose and l-alanine functionalized silicon nanocrystals and their application to cancer cell imaging. *J. Mater. Chem. B* **2014**, *2*, 8427-8433.

(16) Dasog, M.; Bader, K.; Veinot, J. G. C. Influence of halides on the optical properties of silicon quantum dots. *Chem. Mater.* **2015**, *27*, 1153-1156.

(17) Wheeler, L. M.; Neale, N. R.; Chen, T.; Kortshagen, U. R. Hypervalent surface interactions for colloidal stability and doping of silicon nanocrystals. *Nat. Commun.* **2013**, *4*, 2197.

(18) Chen, T.; Skinner, B.; Xie, W.; Shklovskii, B. I.; Kortshagen, U. R. Carrier transport in films of alkyl-ligand-terminated silicon nanocrystals. *J. Phys. Chem. C* **2014**, *118*, 19580-19588.

(19) Liu, C.-Y.; Holman, Z.; Kortshagen, U. Hybrid solar cells from P3HT and silicon nanocrystals. *Nano Lett.* **2009**, *9*, 449-452.

(20) Zhong, Y.; Sun, X.; Wang, S.; Peng, F.; Bao, F.; Su, Y.; Li, Y.; Lee, S. T.; He, Y. Facile, large-quantity synthesis of stable, tunable-color silicon nanoparticles and their application for long-term cellular imaging. *ACS Nano* **2015**, *9*, 5958-5967.

(21) Sugimoto, H.; Furuta, K.; Fujii, M. Controlling energy transfer in silicon quantum dot assemblies made from all-inorganic colloidal silicon quantum dots. *J. Phys. Chem. C* **2016**, *120*, 24469-24475.

(22) Dutt, A.; Matsumoto, Y.; Santana-Rodríguez, G.; Ramos, E.; Monroy, B. M.; Santoyo Salazar, J. Surface chemistry and density distribution influence on visible luminescence of

silicon quantum dots: an experimental and theoretical approach. *Phys. Chem. Chem. Phys.* **2017**, *19*, 1526-1535.

(23) Baldwin, R. K.; Pettigrew, K. A; Ratai, E.; Augustine, M. P.; Kauzlarich, S. M. Solution reduction synthesis of surface stabilized silicon nanoparticles. *Chem. Commun.* **2002**, 1822-1823.

(24) Zou, J.; Kauzlarich, S. M. Functionalization of silicon nanoparticles via silanization: alkyl, halide and ester. *J. Clust. Sci.* **2008**, *19*, 341-355.

(25) Wang, R.; Pi, X.; Yang, D. Surface modification of chlorine-passivated silicon nanocrystals. *Phys. Chem. Chem. Phys.* **2013**, *15*, 1815-1820.

(26) El-Demellawi, J. K.; Holt, C. R.; Abou-Hamad, E.; Al-Talla, Z. A.; Saih, Y.; Chaieb, S. Room-temperature reactivity of silicon nanocrystals with solvents: the case of ketone and hydrogen production from secondary alcohols: catalysis? *ACS Appl. Mater. Interfaces* **2015**, *7*, 13794-13800.

(27) Zhang, Z. H.; Lockwood, R.; Veinot, J. G. C.; Meldrum, A. Detection of ethanol and water vapor with silicon quantum dots coupled to an optical fiber. *Sensors Actuators, B Chem.* **2013**, *181*, 523-528.

(28) Purkait, T. K.; Iqbal, M.; Islam, M. A.; Mobarok, M. H.; Gonzalez, C. M.; Hadidi, L.; Veinot, J. G. C. Alkoxy-terminated Si surfaces: a new reactive platform for the functionalization and derivatization of silicon quantum dots. *J. Am. Chem. Soc.* **2016**, *138*, 7114-7120.

(29) Boukherroub, R.; Morin, S.; Wayner, D. D. M.; Bensebaa, F.; Sproule, G. I.; Baribeau, J.-

M.; Lockwood, D. J. Ideal passivation of luminescent porous silicon by thermal, noncatalytic reaction with alkenes and aldehydes. *Chem. Mater.* **2001**, *13*, 2002-2011.

(30) Hacker, C. A.; Anderson, K. A.; Richter, J. L.; Richter, C. A. Comparison of Si-O-C interfacial bonding of alcohols and aldehydes from dilute solution with ultraviolet irradiation. *Langmuir* **2005**, *21*, 882-889.

(31) Manhat, B. A.; Brown, A. L.; Black, L. A.; Ross, J. B. A.; Fichter, K. One-step melt synthesis of water soluble, photoluminescent, surface-oxidized silicon nanoparticles for cellular imaging applications. *Chem. Mater.* **2011**, *23*, 2407-2418.

(32) Rodríguez, J. A.; Vásquez-Agustín, M. A.; Morales-Sánchez, A.; Aceves-Mijares, M. Emission mechanisms of Si nanocrystals and defects in SiO_2 materials. *J. Nanomater.* **2014**, 409482.

(33) Biteen, J. S.; Lewis, N. S.; Atwater, H. A.; Polman, A. Size-dependent oxygen-related electronic states in silicon nanocrystals. *Appl. Phys. Lett.* **2004**, *84*, 5389-5391.

(34) Takeoka, S.; Fujii, M.; Hayashi, S. Size-dependent photoluminescence from surface-oxidized Si Nanocrystals in a weak confinement regime. *Phys. Rev. B* **2000**, *62*, 16820-16825.

(35) Kanemitsu, Y. Photoluminescence spectrum and dynamics in oxidized silicon nanocrystals: a nanoscopic disorder system. *Phys. Rev. B* **1996**, *53*, 13515-13520.

(36) Dohnalová, K.; Ondič, L.; Kůsová, K.; Pelant, I.; Rehspringer, J. L.; Mafouana, R. R. White-emitting oxidized silicon nanocrystals: discontinuity in spectral development with reducing size. *J. Appl. Phys.* **2010**, *107*, 053102.

(37) Kanemitsu, Y.; Okamoto, S.; Otobe, M.; Oda, S. Photoluminescence mechanism in surface-oxidized silicon nanocrystals. *Phys. Rev. B* **1997**, *55*, 7375-7378.

(38) Wang, R.; Pi, X.; Yang, D. Surface modification of chlorine-passivated silicon nanocrystals. *Phys. Chem. Chem. Phys.* **2013**, *15*, 1815-1820.

(39) Dasog, M.; Veinot, J. G. C. Solid-state synthesis of luminescent silicon nitride nanocrystals. *Chem. Commun.* **2012**, *48*, 3760-3762.

(40) Lin, D. S.; Ku, T. S.; Sheu, T. J. Thermal reactions of phosphine with Si(100): a combined photoemission and scanning-tunneling-microscopy study. *Surf. Sci.* **1999**, *424*, 7-18.

(41) Bennett, J. M.; Warschkow, O.; Marks, N. A.; McKenzie, D. R. Diffusion pathways of phosphorus atoms on silicon (001). *Phys. Rev. B* **2009**, *79*, 165311.

(42) Warschkow, O.; Curson, N. J.; Schofield, S. R.; Marks, N. A.; Wilson, H. F.; Radny, M. W.; Smith, P. V.; Reusch, T. C. G.; McKenzie, D. R.; Simmons, M. Y. Reaction paths of phosphine dissociation on silicon (001). *J. Chem. Phys.* **2016**, *144*, 14705.

(43) Sweryda-Krawiec, B.; Cassagneau, T.; Fendler, J. H. Surface modification of silicon nanocrystallites by alcohols. *J. Phys. Chem. B* **1999**, *103*, 9524-9529.

(44) Sweryda-Krawiec, B.; Chandler-Henderson, R. R.; Coffer, J. L.; Rho, Y. G.; Pinizzotto, R. F. A comparison of porous silicon and silicon nanocrystallite photoluminescence quenching with amines. *J. Phys. Chem.* **1996**, *100*, 13776-13780.

(45) Sailor, M. J.; Wu, E. C. Photoluminescence-based sensing with porous silicon. *Adv. Funct. Mater.* **2009**, *19*, 3195-3208.

(46) Mitchell, S. A.; Boukherroub, R.; Anderson, S. Second harmonic generation at chemically

modified Si(111) surfaces. *J. Phys. Chem. B* **2000**, *104*, 7668–7676.

(47) Haber, J. A.; Lewis, N. S. Infrared and X-ray photoelectron spectroscopic studies of the reactions of hydrogen-terminated crystalline Si(111) and Si(100) surfaces with Br_2, I_2, and ferrocenium in alcohol solvents. *J. Phys. Chem. B* **2002**, *106*, 3639-3656.

(48) Plymale, N. T.; Dasog, M.; Brunschwig, B. S.; Lewis, N. S. A mechanistic study of the oxidative reaction of hydrogen-terminated Si(111) surfaces with liquid methanol. *J. Phys. Chem. C* **2017**, *121*, 4270-4282.

(49) Dasog, M.; Rachinsky, C.; Veinot, J. G. C. From Si and C encapsulated SiO_2 to SiC: exploring the influence of sol-gel polymer substitution on thermally induced nanocrystal formation. *J. Mater. Chem.* **2011**, *21*, 12422-12427.

(50) Henderson, E. J.; Kelly, J. A.; Veinot, J. G. C. Influence of $HSiO_{1.5}$ sol-gel polymer structure and composition on the size and luminescent properties of silicon nanocrystals. *Chem. Mater.* **2009**, *21*, 5426-5434.

(51) Escorihuela, J.; Zuilhof, H. Rapid surface functionalization of hydrogen-terminated silicon by alkyl silanols. *J. Am. Chem. Soc.* **2017**, *139*, 5870-5876.

(52) Sublemontier, O.; Nicolas, C.; Aureau, D.; Patanen, M.; Kintz, H.; Liu, X.; Gaveau, M. A.; Le Garrec, J. L.; Robert, E.; Barreda, F. A.; Etcheberry, A.; Reynaud, C.; Mitchell, J. B.; Miron, C. X-ray photoelectron spectroscopy of isolated nanoparticles. *J. Phys. Chem. Lett.* **2014**, *5*, 3399-3403.

(53) Hajjaji, H.; Alekseev, S.; Guillot, G.; Blanchard, N. P.; Monnier, V.; Chevolot, Y.; Brémond, G.; Querry, M.; Philippon, D.; Vergne, P.; Bluet, J. M. Luminescence

nanothermometry with alkyl-capped silicon nanoparticles dispersed in nonpolar liquids. *Nanoscale Res. Lett.* **2014**, *9*, 94.

(54) Terekhov, V. A.; Turishchev, S. Y.; Pankov, K. N.; Zanin, I. E.; Domashevskaya, E. P.; Tetelbaum, D. I.; Mikhailov, A. N.; Belov, A. I.; Nikolichev, D. E.; Zubkov, S. Y. XANES, USXES and XPS investigations of electron energy and atomic structure pecularities of the silicon suboxide thin film surface layers containing Si nanocrystals. *Surf. Interface Anal.* **2010**, *42*, 891-896.

(55) Hessel, C. M.; Rasch, M. R.; Hueso, J. L.; Goodfellow, B. W.; Akhavan, V. A.; Puvanakrishnan, P.; Tunnel, J. W.; Korgel, B. A. Alkyl passivated and amphiphillic polymer coating of silicon nanocrystals for diagnostic imaging. *Small* **2010**, *6*, 2026-2034.

(56) Márquez, F.; Morant, C.; López, V.; Zamora, F.; Campo, T.; Elizalde, E. An alternative route for the synthesis of silicon nanowires via porous anodic alumina masks. *Nanoscale Res. Lett.* **2011**, *6*, 495.

(57) Khung, Y. L.; Ngalim, S. H.; Scaccabarozzi, A.; Narducci, D. Formation of stable Si-O-C submonolayers on hydrogen terminated silicon(111) under low-temperature conditions. *Beilstein J. Nanotechnol.* **2015**, *6*, 19–26.

(58) Yu, Y.; Hessel, C. M.; Bogart, T.; Panthani, M. G.; Rasch, M. R.; Korgel, B. A. Room temperature hydrosilylation of silicon nanocrystals with bifunctional terminal alkenes. *Langmuir* **2014**, *29*, 1533-1540.

(59) Buriak, J. M.; Sikder, M. D. H. From molecules to surfaces: radical-based mechanisms of Si-S and Si-Se bond formation on silicon. *J. Am. Chem. Soc.* **2015**, *137*, 9730-9738.

(60) Hu, M.; Liu, F.; Buriak, J. M. Expanding the repertoire of molecular linkages to silicon: Si-S, Si-Se, and Si-Te bonds. *ACS Appl. Mater. Interfaces* **2016**, *8*, 11091-11099.

(61) Conibeer, G.; Green, M.; Cho, E. C.; König, D.; Cho, Y. H.; Fangsuwannarak, T.; Scardera, G.; Pink, E.; Huang, Y.; Puzzer, T.; Huang, S.; Song, D.; Flynn, C.; Park, S.; Hao, X.; Mansfield, D. Silicon quantum dot nanostructure for tandem photovoltaic cells. *Thin Solid Films* **2008**, *516*, 6748-6756.

(62) Macias-Montero, M.; Askari, S.; Mitra, S.; Rocks, C.; Ni, C.; Svrcek, V.; Connor, P. A.; Maguire, P.; Irvine, J. T. S.; Mariotti, D. Energy band diagram of device-grade silicon nanocrystals. *Nanoscale* **2016**, *8*, 6623-6628.

(63) Botas, A. M. P.; Ferreira, R. a. S.; Pereira, R. N.; Anthony, R. J.; Moura, T.; Rowe, D. J.; Kortshagen, U. R. High quantum yield dual-emission from gas phase grown crystalline Si nanoparticles. *J. Phys. Chem. C* **2014**, *118*, 10375-10383.

(64) Mitra, S.; Švrček, V.; Macias-Montero, M.; Velusamy, T.; Mariotti, D. Temperature-dependent photoluminescence of surface-engineered silicon nanocrystals. *Sci. Rep.* **2016**, *6*, 27727.

(65) Wolf, O.; Dasog, M.; Yang, Z.; Balberg, I.; Veinot, J. G. C.; Millo, O. Doping and quantum confinement effects in single Si nanocrystals observed by scanning tunneling spectroscopy. *Nano Lett.* **2013**, *13*, 2516-2521.

(66) Ramos, E.; Monroy, B. M.; Alonso, J. C.; Sansores, L. E.; Salcedo, R.; Mart, A. Theoretical study of the electronic properties of silicon nanocrystals partially passivated with Cl and F. *J. Phys. Chem. C* **2012**, *116,* 3988-3994.

(67) Furukawa, S.; Miyasato, T. Quantum size effects on the optical band gap of microsrystalline Si:H. *Phys. Rev. B* **1988**, *38*, 5726-5729.

(68) Hill, N. A.; Whaley, K. B. Size dependence of excitons in silicon nanocrytals. *Phys. Rev. Lett.* **1995**, *75*, 1130-1133.

(69) Ouyang, J.; Bard, A. J. Inverse photoemission spectroscopy at metal/acetonitrile interface by hole injection through solution species. *J. Phys. Chem.* **1988**, *92*, 5201-5205.

(70) Wheeler, L. M.; Anderson, N. C.; Palomaki, P. K. B.; Blackburn, L.; Johnson, J. C.; Neale, N. R. Silyl radical abstraction in the functionalization of plasma-synthesized silicon nanocrytals. *Chem. Mater.* **2015**, *27*, 6869-6878.

(71) Kelly, J. A.; Shukaliak, A. M.; Fleischauer, M. D.; Veinot, J. G. C. Size-dependent reactivity in hydrosilylation of silicon nanocrytals. *J. Am. Chem. Soc.* **2011**, *133*, 9564-8571.

(72) Reboredo, F. A.; Schwegler, E.; Galli, G. Optically activated functionalization reactions in Si quantum dots. *J. Am. Chem. Soc.* **2003**, *125*, 15243-15249.

(73) Mastronardi, M. L.; Chen, K. K.; Liao, K.; Casillas, G.; Ozin, G. A. Size-dependent chemical reactivity of silicon nanocrystals with water and oxygen. *J. Phys. Chem. C* **2015**, *119*, 826-834.

(74) Yang, Z.; De Los Reyes, G. B.; Titova, L. V.; Sychugov, I.; Dasog, M.; Linnros, J.; Hegmann, F. A.; Veinot, J. G. C. Evolution of the ultrafast photoluminescence of colloidal silicon nanocrystals with changing surface chemistry. *ACS Photonics* **2015**, *2*, 595-605.

(75) De los Reyes, G. B.; Dasog, M.; Na, M.; Titova, L. V; Veinot, J. G. C.; Hegmann, F. A.

Charge transfer state emission dynamics in blue-emitting functionalized silicon nanocrystals. *Phys. Chem. Chem. Phys.* **2015**, *17*, 30125-30133.

(76) Cucinotta, C.; Ruini, A.; Caldas, M. J.; Molinari, E. Abinitio study of chemisorption reactions for carboxylic acids on hydrogenated silicon surfaces. *J. Phys. Chem. B* **2004**, *108*, 17278-17280.

(77) Hessel, C. M.; Reid, D.; Panthani, M. G.; Rasch, M. R.; Goodfellow, B. W.; Wei, J.; Fujii, H.; Akhavan, V.; Korgel, B. A. Synthesis of ligand-stabilized silicon nanocrystals with size-dependent photoluminescence spanning visible to near-infrared wavelengths. *Chem. Mater.* **2012**, *24*, 393-401.

(78) Lorentz, B. Y.; Pihl, A. The equilibrium constants and oxidation-reduction potentials of some thiol-disulfide systems. *Science* **1957**, *79*, 4589-4593.

TOC graphic

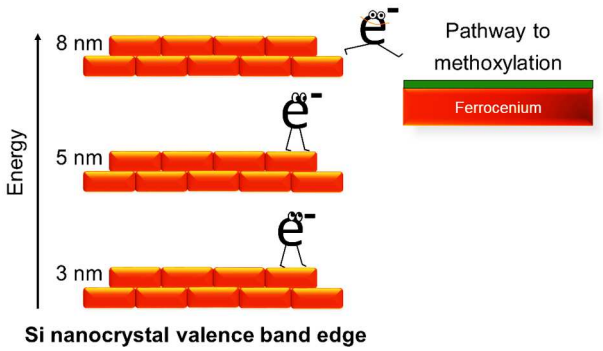
8 nm
5 nm
3 nm
Energy
Pathway to
methoxylation
Ferrocenium
Si nanocrystal valence band edge